

Article

Effective Degradation of Metronidazole through Electrochemical Activation of Peroxymonosulfate: Mechanistic Insights and Implications

Haicen Liao ^{1,†}, Jingkai Fang ^{1,†}, Jiahao Wang ¹, Xianhu Long ¹, Igor Ying Zhang ^{2,*} and Rongfu Huang ^{1,*}

¹ Sichuan Provincial Key Laboratory of Universities on Environmental Science and Engineering, MOE Key Laboratory of Deep Earth Science and Engineering, College of Architecture and Environment, Sichuan University, Chengdu 610065, China

² Collaborative Innovation Centre of Chemistry for Energy Materials, Shanghai Key Laboratory of Molecular Catalysis and Innovation Materials, MOE Laboratory for Computational Physical Science, Shanghai Key Laboratory of Bioactive Small Molecules, Department of Chemistry, Fudan University, Shanghai 200433, China

* Correspondence: igor_zhangying@fudan.edu.cn (I.Y.Z.); rongfu@scu.edu.cn (R.H.)

† These authors contributed equally to this work.

Abstract: The investigation into the degradation of metronidazole (MNZ), a frequently employed antibiotic, through the electrochemical activation of peroxymonosulfate (PMS) utilizing either boron-doped diamond (BDD) or dimensional stable anode (DSA) as the anode, was conducted in a systematic manner. The enhancement of MNZ removal was observed with increasing current density, PMS dosage, and initial pH. Response surface methodology (RSM), based on a Box–Benken design, was utilized to evaluate the efficiency of MNZ elimination concerning current density (ranging from 11.1 to 33.3 mA/cm²), initial pH (ranging from 3 to 9), PMS dosage (ranging from 1 to 5 mmol·L⁻¹), and reaction time (ranging from 25 to 45 min). The optimal operational conditions for MNZ removal were determined as follows: a current density of 13.3 mA/cm², a pH of 3.7, a PMS dosage of 2.4 mmol·L⁻¹, and a reaction time of 40 min. Electron paramagnetic resonance (EPR), quenching experiments, and chemical probe experiments confirmed the involvement of $\bullet\text{OH}$, $\text{SO}_4^{\bullet-}$ and $^1\text{O}_2$ radicals as the primary reactive species in MNZ degradation. The presence of HCO_3^- and H_2PO_4^- hindered MNZ removal, whereas the presence of Cl^- accelerated it. The degradation pathways of MNZ were elucidated by identifying intermediates and assessing their toxicity. Additionally, the removal efficiencies of other organic pollutants, such as sulfamethoxazole (SMX), carbamazepine (CBZ), and nitrobenzene (NB), were compared. This study contributes to a comprehensive understanding of MNZ degradation efficiency, mechanisms, and pathways through electrochemical activation of PMS employing BDD or DSA anodes, thereby offering valuable insights for the selection of wastewater treatment systems.

Keywords: electrolysis; electrochemical activation; peroxymonosulfate; metronidazole; water treatment



Citation: Liao, H.; Fang, J.; Wang, J.; Long, X.; Zhang, I.Y.; Huang, R.

Effective Degradation of Metronidazole through Electrochemical Activation of Peroxymonosulfate: Mechanistic Insights and Implications. *Energies* **2024**, *17*, 1750. <https://doi.org/10.3390/en17071750>

Academic Editor: Antonino S. Arico

Received: 19 February 2024

Revised: 2 April 2024

Accepted: 2 April 2024

Published: 5 April 2024



Copyright: © 2024 by the authors. Licensee MDPI, Basel, Switzerland. This article is an open access article distributed under the terms and conditions of the Creative Commons Attribution (CC BY) license (<https://creativecommons.org/licenses/by/4.0/>).

1. Introduction

Metronidazole (MNZ) serves as a widely employed antibiotic used in the treatment of anaerobic bacterial infections, bacteroides, and protozoal infections among humans [1]. Despite its medical utility, MNZ has been recurrently detected in various environmental matrices, including drinking water, groundwater, surface water, soil sediments, and wastewater [1–3]. Concerns regarding MNZ's presence in these environments stem from its potential carcinogenic and mutagenic properties, particularly when administered in elevated doses [4,5]. Moreover, MNZ poses a significant threat to human health due to its neural toxic effects [6,7]. Its intricate chemical composition, coupled with characteristics such as high solubility, microbial toxicity, and challenging biodegradability [8–10], signifies

the difficult task of removing MNZ from water and wastewater. Traditional water treatment methods struggle to effectively eliminate MNZ [6,11,12], highlighting an urgent need for the development of robust techniques with high degradation efficiency to completely eradicate MNZ from contaminated environments.

In the recent decade, advanced oxidation processes (AOPs) have gained significant attention for their efficacy in eliminating types of organic contaminants. Notably, electrochemical advanced oxidation processes (EAOPs) and sulfate-radical-related AOPs ($\text{SO}_4^{\bullet-}$ -AOPs) have emerged as promising methodologies [13–15]. In EAOPs, a wide range of organic pollutants are eradicated through electron exchange or the generation of oxidizing radicals, primarily hydroxyl radicals ($\bullet\text{OH}$) [16]. EAOPs present several advantages over conventional methods: (I) operations can be conducted at ambient temperature and pressure, with electrochemical systems offering automation feasibility and requiring minimal floor space [17,18]; (II) EAOPs are environmentally friendly, utilizing clean reagents like electrons, and some processes, such as electro-oxidation, necessitate only electricity without further treatment for contaminant degradation [18,19]; (III) the versatility of EAOPs enables their integration with various techniques for organic pollutant removal, thereby facilitating a broad range of relevant applications [17,20].

Conversely, $\text{SO}_4^{\bullet-}$ -AOPs, which generate $\text{SO}_4^{\bullet-}$, represent promising and effective alternatives for target compound treatment [21]. With a robust oxidation potential (2.6 V) and a longer half-life compared to $\bullet\text{OH}$ [22,23], $\text{SO}_4^{\bullet-}$ shows considerable potential. Presently, the predominant method for $\text{SO}_4^{\bullet-}$ generation involves the activation of persulfate (peroxydisulfate (PDS) and peroxymonosulfate (PMS)) [24]. PS activation can theoretically occur through electron transfer and energy excitation mechanisms [25], with activation achievable via diverse means such as heat, UV photolysis, alkaline conditions, transition metals, and ultrasound [26–35]. Given the simplicity and minimal secondary pollution associated with EAOPs, electrochemical activation of PS emerges as an ideal alternative due to its clean reaction products and comparatively lower energy consumption relative to other activation methods [24]. While both PDS and PMS can be electrochemically activated, PMS exhibits higher efficiency in degrading organic pollutants, possibly attributable to its asymmetrical peroxide bond with a partial positive charge [24,36]. Consequently, the widespread exploration of PMS-based $\text{SO}_4^{\bullet-}$ -AOPs for contaminated wastewater treatment has been observed, given PMS's advantageous attributes such as high aqueous solubility, subsurface stability, cost-effectiveness, and benign end products [23,37,38]. Additionally, numerous studies have highlighted the significance of direct electron transfer (DET) reactions in contaminant degradation [39–41]. Considering the potentially synergistic effects and mechanisms of EAOPs, SAOPs systems, and DET processes in organic pollutant degradation, further attention and comprehensive assessments are warranted.

Various investigations have indicated a range of outcomes regarding the efficacy of dimensionally stable anodes (DSA) in degrading contaminants. DSAs are fabricated through the deposition of a thin layer of metal oxides, typically RuO_2 - and IrO_2 -based coatings, onto a base metal, commonly titanium [42]. However, these metal oxides demonstrate limited reactivity toward organic oxidation [43–45]. In contrast, boron-doped diamond (BDD) has emerged as a promising anode material for degrading organic contaminants in EAOPs. This is attributed to BDD's high oxygen evolution over-potential, exceptional electrochemical performance, mechanical durability, and chemical inertness [24,46,47].

The objectives of this study are fourfold:

- (i) To examine the influence of operational parameters, specifically current density and PMS dosage, on the degradation efficiency of EC-PMS-BDD and EC-PMS-DSA systems (EC is the abbreviation of the electrochemical system).
- (ii) To systematically investigate the sources and generation of reactive oxygen species (ROS), including $\bullet\text{OH}$, $\text{SO}_4^{\bullet-}$, and $^1\text{O}_2$ in these processes, elucidating their respective oxidation mechanisms.
- (iii) To utilize the Box–Behnken Design model to assess the optimal conditions leading to the highest MNZ removal efficiency.

- (iv) To analyze the structural characteristics of MNZ byproducts generated during the degradation processes and evaluate the environmental implications concerning other organic pollutants.

2. Materials and Methods

2.1. Materials

All chemicals utilized in this study are listed in Appendix A.

2.2. Experimental Setup and Procedures

The MNZ degradation experiments were conducted under a constant current provided by a DC power source (APS3005S-3D, GRATTEN, Shanghai, China). Unless otherwise specified, a current density of 33.3 mA/cm² was maintained for the electrolysis activation process. The reactor employed for the experiments consisted of a 250 mL glass beaker containing 160 mL of MNZ solution at a concentration of 80 µmol·L⁻¹. Meanwhile, 20 mmol·L⁻¹ of Na₂SO₄ was incorporated as the supporting electrolyte, while NaOH and H₂SO₄ were employed for pH adjustment. A predetermined quantity of PMS (1 mmol·L⁻¹) was added to the solution, which was continuously stirred at room temperature (around 25 °C).

BDD or DSA electrodes, measuring 3 cm × 3 cm × 0.1 cm, were utilized as the anode, whereas graphite electrodes of the same dimensions served as the cathode, both possessing effective working areas of 9 cm². Positioned in parallel, the anode and cathode were situated at a distance of 2 cm from each other. At specific time intervals (0, 5, 10, 15, 20, 30, and 45 min), 1 mL of the sample was withdrawn from the reactor and transferred to a sample vial containing 10 µL of 0.1 mmol·L⁻¹ Na₂S₂O₃ solution to quench reactive radicals within the sample. All experiments were performed in duplicate, and the resultant average values were computed, accompanied by error bars to denote variability.

2.3. Analytical Methods

A UV-vis spectroscopy (UV-3600, Shimadzu, Kyoto, Japan) was utilized to monitor the concentration of PMS at a wavelength of 735 nm. Electron paramagnetic resonance (EPR) spectroscopy (EPR200-Plus, CIQTEK, Hefei, China) operating at continuous wave X band frequency was used to detect the radicals ([•]OH, SO₄^{•-}, and ¹O₂) generated during the degradation process. High-performance liquid chromatography (HPLC, Agilent 1260, Agilent, Santa Clara, CA, USA) equipped with an Eclipse XDB C-18 column (5 µm, 250 × 4.6 mm, Agilent) was employed to quantify the concentration of MNZ and other organic compounds. Comprehensive details regarding the HPLC methods are delineated in Appendix B and Table 1. The transformation products resulting from MNZ degradation were identified using ultrahigh-performance liquid chromatography–quadrupole time-of-flight mass spectrometry (UHPLC-QTOF-MS, Agilent 6545, Santa Clara, USA). A 10 µL injection volume and a flow rate of 0.2 mL min⁻¹ were applied. The mobile phase comprised a mixture of ultrapure water (designated as A) and acetonitrile (B) at a ratio of 25:75.

Table 1. Parameters of HPLC methods for analysis of different compounds.

Compound	Wavelength (nm)	Mobile Phase A		Mobile Phase B	
		Ultrapure Water (%)	0.1% (v/v) Acetic Acid Solution (%)	Acetonitrile (%)	Methyl Alcohol (%)
MNZ	318	80	N.A.	20	N.A.
SMX	265	N.A.	60	40	N.A.
CBZ	284	60	N.A.	40	N.A.
BA	230	50	N.A.	50	N.A.
NB	262	N.A.	50	50	N.A.
<i>p</i> -HBA/ <i>p</i> -BQ	246	70	N.A.	30	N.A.

3. Results

3.1. Removal Efficiency of MNZ in Various Processes

The degradation of MNZ across various processes is depicted in Figure 1. As illustrated in Figure 1, the MNZ removal efficiency stood at 2.9% and 5.8% for the adsorption process employing boron-doped diamond (BDD) and dimensionally stable anode (DSA), respectively. These modest degradation rates suggest a minimal adsorption effect exerted by both BDD and DSA anodes. Furthermore, MNZ degradation through PMS alone remained negligible at 4.9%.

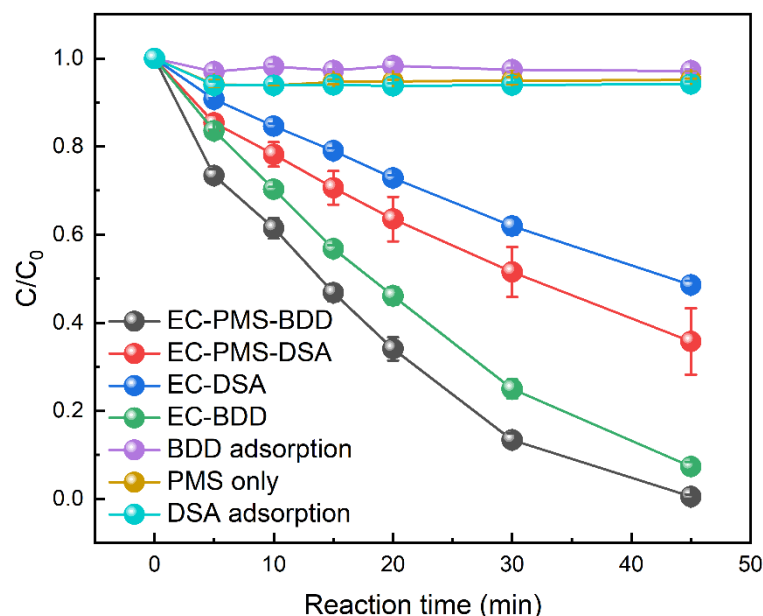
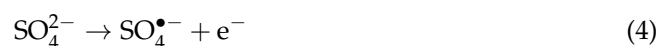
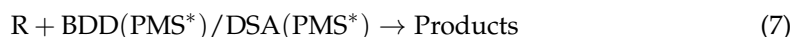
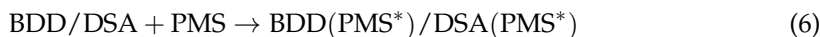


Figure 1. The degradation of MNZ in different systems. Reaction conditions: $[MNZ] = 80 \mu\text{mol}\cdot\text{L}^{-1}$, $[\text{Na}_2\text{SO}_4] = 20 \text{mmol}\cdot\text{L}^{-1}$, $\text{pH}_0 = 6$, $[\text{PMS}] = 1 \text{mmol}\cdot\text{L}^{-1}$, $I = 33.3 \text{mA}/\text{cm}^2$.

Moreover, the MNZ removal efficiency via electrolysis alone with a BDD anode (92.7%) surpassed that with a DSA anode (51.7%), underscoring the superior efficacy of BDD anodes in MNZ removal compared to DSA anodes. The substantial MNZ removal rates observed in both EC-BDD (92.7%) and EC-DSA (51.7%) systems indicate the involvement of DET processes (Equation (1)) and electrolysis utilizing BDD or DSA anodes to yield oxygen (Equation (2)) or $\bullet\text{OH}$ (Equation (3)) [39]. Additionally, the electrochemical activation of PMS to form $\text{SO}_4^{\bullet-}$ (Equation (4)) contributed to MNZ degradation [48]. The incorporation of PMS into the electrolytic reactor augmented MNZ degradation to 99.5% on BDD and 64.3% on DSA anodes, respectively. This enhancement can be attributed to the activation of PMS via electrolysis on both BDD and DSA anodes, generating $\bullet\text{OH}$ and $\text{SO}_4^{\bullet-}$ (Equation (5)) [49]. Furthermore, the observed increase in MNZ removal efficiency may be attributed to the conversion of a fraction of PMS into a specialized transition state structure (PMS^* , Equation (6)) through anodic discharge. PMS^* exhibits the capability to degrade organic contaminants, functioning as a nonradical oxidation pathway (Equation (7)) [39]. These findings align with the observed decrease in PMS concentration depicted in Figure S1.





3.2. Optimization of Electrochemical Reaction Parameters

3.2.1. Effect of Current Density

The current density proved to be a pivotal parameter in the electro-oxidation process, as demonstrated in Figure 2a. Investigation into the effect of applied current revealed notable trends (Figure 2a). Specifically, when a current density of 44.4 mA/cm² was applied for a duration of 30 min, MNZ degradation reached 100%, surpassing the degradation achieved with 33.3 mA/cm² (87.6%) on BDD (Figure S2a). Conversely, on DSA, only 55.4% of MNZ was removed (Figure S2d). These findings indicate a significant dependency of MNZ removal efficiency on current density.

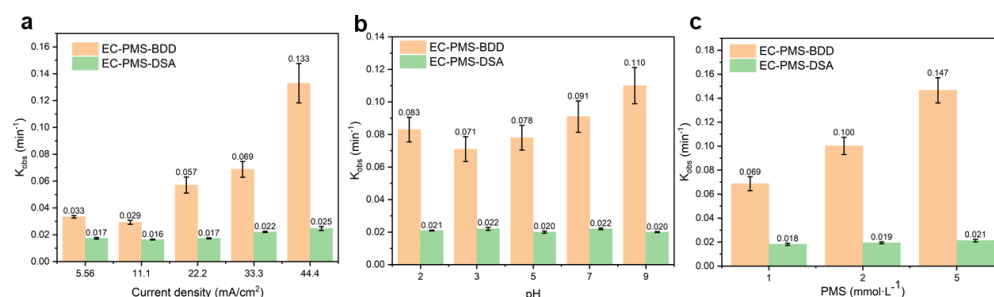


Figure 2. Comparison of EC-PMS-BDD system and EC-PMS-DSA system in pseudo-first-order kinetic constant: (a) current density, (b) pH, and (c) PMS dosage. Reaction conditions: [MNZ] = 80 μmol·L⁻¹, [Na₂SO₄] = 20 mmol·L⁻¹, pH₀ = 6, [PMS] = 1 mmol·L⁻¹, and I = 33.3 mA/cm².

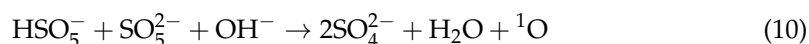
Furthermore, the results illustrate that MNZ removal decreased from 78.3% to 72.3% as current density increased from 5.5 to 11.1 mA/cm² on the BDD anode, with a concomitant decline in the rate constant from 0.033 to 0.029 min⁻¹ (Figure 2a). It is due to the occurrence of undesired oxygen evolution reaction (OER) under low current conditions. When the current density increases, there are more active species being produced in the system to diminish the OER effect on the degradation process. Despite efforts to minimize OER using BDD electrodes, oxygen production still transpires as follows (Equations (8) and (9)) [50]. Moreover, an analysis of MNZ removal processes using a pseudo-first-order kinetics model (Figure S3a–d) revealed rate constants of 0.133 min⁻¹ and 0.025 min⁻¹ when the current density was 44.4 mA/cm² on BDD and DSA anodes, respectively. These results underscore the pronounced influence of current density on the electro-oxidation process and highlight the superior performance of BDD anodes compared to DSA counterparts.



3.2.2. Effect of Initial pH

The removal efficiency of MNZ by EC-PMS-BDD and EC-PMS-DSA systems was examined across various initial pH values (Figure S2b–e). When the initial pH was set at 6, the final pH was measured as 3.2 due to the occurrence of oxygen evolution reaction (OER), which explains the oxygen bubbles observed in the experiment. Notably, MNZ removal increased from 83.7% to 96.4% as the initial pH rose from 2 to 9 within a 30 min timeframe on the BDD anode. Conversely, MNZ removal remained stable on the DSA anode, indicating a gradual generation of singlet oxygen (¹O₂) through PMS self-decomposition under alkaline conditions (Equation (10)) [49,51–53]. Notably, ¹O₂ is postulated to act as a crucial oxidizing species, bolstering MNZ removal. It is worth mentioning that the reaction of Equation (10)

may also occur on the BDD anode, and the experimental results are the sum of all reactions occurring in the individual system.



3.2.3. Effect of PMS Dosage

In the electrochemical activation of the PMS process, the concentration of PMS plays a crucial role in MNZ degradation owing to the generation of $\bullet\text{OH}$ and $\text{SO}_4^{\bullet-}$. Consequently, MNZ removal at various PMS concentrations was investigated. As depicted in Figure S2c, MNZ degradation exhibited acceleration with increasing PMS concentration. Specifically, MNZ removal escalated from 86.6% to 99.0% as PMS concentration increased from 1 to 5 $\text{mmol}\cdot\text{L}^{-1}$ on the BDD anode within a 30 min duration, accompanied by an elevation in the rate constant from 0.069 to 0.147 min^{-1} (Figure 2c). Conversely, in the EC-PMS-DSA system, although MNZ removal efficiency exhibited a mild increase (57.9% to 63.8%) as PMS concentration rose from 1 to 5 $\text{mmol}\cdot\text{L}^{-1}$ (Figure S2f), which nonetheless facilitated MNZ degradation. This outcome can be attributed to the heightened production of reactive species with increasing PMS concentration, thereby fostering MNZ removal. Analogous conclusions have been drawn in studies concerning the degradation of tetracycline (TC) [54] and norfloxacin (NOR) [55].

3.3. Optimum Conditions by RSM

The synergistic effects of various operating conditions are often considered paramount in achieving optimal removal efficiency. Therefore, response surface methodology (RSM) was employed to identify the optimal operating conditions by exploring the synergistic effects of four parameters: current density, initial pH, PMS dosage, and reaction time. Building upon the outcomes of the univariate experiments detailed earlier (Section 3.2), the range of each parameter is delineated in Table 2.

Table 2. Actual values corresponding to coded levels of RSM.

Coded Levels	A: Current Density (mA/cm^2)	B: Initial pH	C: PMS Dosage ($\text{mmol}\cdot\text{L}^{-1}$)	D: Reaction Time (min)
−1 (Low)	11.1	3	1	25
0 (Medium)	22.2	6	3	35
1 (High)	33.3	9	5	45

The experimental design, employing a four-factor and three-level response surface optimization, was conducted using the Box–Behnken Design (BBD) method, comprising 29 experimental runs (Table 3). The results of the analysis of variance are presented in Table 3. For RSM analysis, we used the software “Design expert” v8.0.5 to optimize multiple conditions based on their respective influence on the removal efficiency of MNZ. And Equation (11) was generated automatically by the software based on the conditions in Table 3. The coefficients indicate the impact of individual parameters on the response; the positive numbers represent the positive impact while negative numbers represent the negative impact.

$$\begin{aligned} (C_0 - C)/C_0 = & 0.94 + 0.12 \times A - 0.020 \times B + 0.073 \times C + 0.10 \times D \\ & + 0.0054 \times AB - 0.037 \times AC - 0.050 \times AD + 0.00052 \times BC \\ & + 0.020 \times BD - 0.027 \times CD - 0.055 \times A^2 + 0.00073 \times B^2 \\ & - 0.047 \times C^2 - 0.057 \times D^2 \end{aligned} \quad (11)$$

where A is the current density, B is the initial pH, C is the PMS dosage, and D is the reaction time. The equation (Equation (11)) in terms of coded factors can be used to make predictions about the response for the given levels of each factor. The coded equation is useful for identifying the relative impact of the factors by comparing the factor coefficients.

Table 3. The 4-factor Box–Behnken design of RSM and experimental response.

Standard Order	Run Order	Current Density (mA/cm ²)	pH (1)	PMS Dosage (mmol·L ⁻¹)	Reaction Time (min)	MNZ Removal Rate (1)
8	1	22.2	6	5	45	1
2	2	33.3	3	3	35	1
27	3	22.2	6	3	35	0.94103
23	4	22.2	3	3	45	1
19	5	11.1	6	5	35	0.86044
26	6	22.2	6	3	35	0.9398
22	7	22.2	9	3	25	0.74029
29	8	22.2	6	3	35	0.9407
15	9	22.2	3	5	35	0.98338
28	10	22.2	6	3	35	0.9426
3	11	11.1	9	3	35	0.76985
14	12	22.2	9	1	35	0.78515
4	13	33.3	9	3	35	0.98794
17	14	11.1	6	1	35	0.6179
11	15	11.1	6	3	45	0.79368
16	16	22.2	9	5	35	0.92868
5	17	22.2	6	1	25	0.6271
20	18	33.3	6	5	35	0.9948
18	19	33.3	6	1	35	0.9013
9	20	11.1	6	3	25	0.54074
25	21	22.2	6	3	35	0.9412
21	22	22.2	3	3	25	0.81912
12	23	33.3	6	3	45	0.99603
24	24	22.2	9	3	45	1
10	25	33.3	6	3	25	0.94412
6	26	22.2	6	5	25	0.805
13	27	22.2	3	1	35	0.84191
1	28	11.1	3	3	35	0.80368
7	29	22.2	6	1	45	0.9258

From the Prob > F values presented in Table 4, also known as the p values, it is evident that the p value associated with the initial pH (0.0450) meets the criterion of $0.01 < p < 0.05$. This suggests that the initial pH significantly influences the parameter $(C_0 - C)/C_0$. Consequently, it was deemed unnecessary to exclude this influential factor from further analysis. However, it is worth noting that the initial pH was not as statistically significant as the other three factors ($p < 0.01$).

Table 4. ANOVA analysis for MNZ removal efficiency.

Source	Sum of Squares	df	Mean Square	F-Value	<i>p</i> Value Prob > F	
Model	0.43	14	0.031	32.24	<0.0001	significant
A-current density	0.17	1	0.17	179.54	<0.0001	
B-initial pH	4.648×10^{-3}	1	4.648×10^{-3}	4.84	0.0450	
C-initial PMS concentration	0.064	1	0.064	65.79	<0.0001	
D-reaction time	0.13	1	0.13	133.92	<0.0001	
AB	1.185×10^{-4}	1	1.185×10^{-4}	0.12	0.7305	
AC	5.553×10^{-3}	1	5.553×10^{-3}	5.79	0.0305	
AD	0.010	1	0.010	10.53	0.0059	
BC	1.061×10^{-6}	1	1.061×10^{-6}	1.106×10^{-3}	0.9739	
BD	1.554×10^{-3}	1	1.554×10^{-3}	1.62	0.2240	
CD	2.830×10^{-3}	1	2.830×10^{-3}	2.95	0.1079	
A ²	0.020	1	0.020	20.79	0.0004	
B ²	3.487×10^{-6}	1	3.487×10^{-6}	3.634×10^{-3}	0.9528	
C ²	0.015	1	0.015	15.25	0.0016	
D ²	0.021	1	0.021	22.30	0.0003	
Residual	0.013	14	9.596×10^{-4}			
Lack of Fit	0.013	10	1.343×10^{-3}	1307.41	<0.0001	significant
Pure Error	4.109×10^{-6}	4	1.027×10^{-6}			
Cor Total	0.45	28				

Based on the observed *p* values, the order of significance of the effects of the four influencing factors can be listed as follows: current density > reaction time > PMS dosage > initial pH. This ranking highlights the varying degrees of impact exerted by each factor on MNZ degradation.

The interaction between these factors on MNZ degradation by the BDD anode is depicted in Figure 3, providing visual insight into the synergistic effects and their implications for MNZ removal.

The optimal experimental conditions for the degradation of metronidazole (MNZ) in simulated wastewater using the EC-PMS-BDD system were predicted by the model. Under these predicted conditions, with an initial MNZ concentration of $80 \mu\text{mol}\cdot\text{L}^{-1}$, a current density of $13.3 \text{ mA}/\text{cm}^2$, an initial pH of 3.7, and a PMS dosage of $2.4 \text{ mmol}\cdot\text{L}^{-1}$, MNZ removal reached 100% within 40 min. To validate the predictive accuracy of the model, experimental verification was conducted under the aforementioned conditions, resulting in an MNZ removal efficiency of 100%. This experimental outcome aligns perfectly with the predicted value, thereby affirming the accuracy and reliability of the Box–Behnken model for optimizing MNZ degradation in the EC-PMS-BDD system and predicting experimental results.

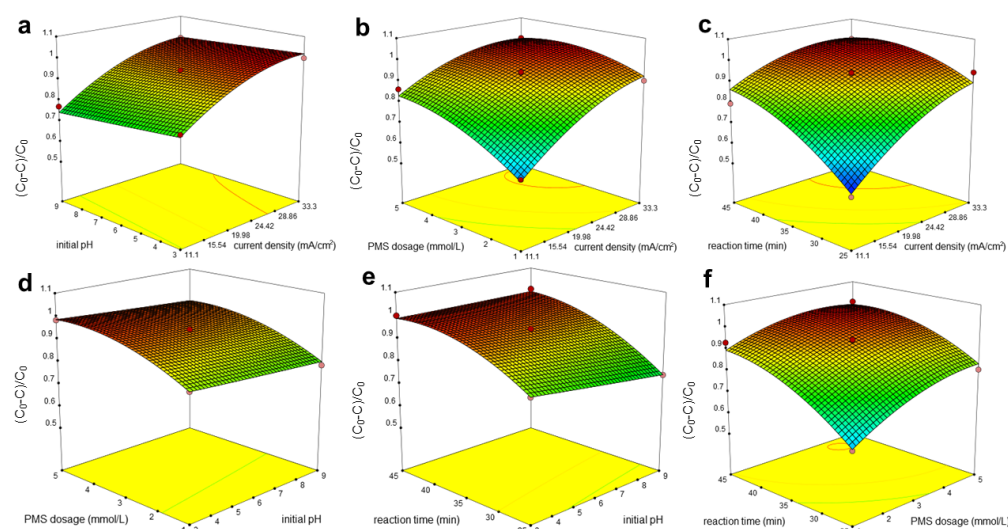


Figure 3. Response surface plot of the effects of (a) current density vs. initial pH, (b) current density vs. PMS dosage, (c) current density vs. reaction time, (d) initial pH vs. PMS dosage, (e) initial pH vs. reaction time, and (f) PMS dosage vs. reaction time.

3.4. Mechanism Study

3.4.1. EPR Test

An electron paramagnetic resonance (EPR) test using DMPO and TEMP as spin-trapping agents was applied to detect the $\bullet\text{OH}$, $\text{SO}_4^{\bullet-}$ and $^1\text{O}_2$ generated during the EC process [56,57]. As illustrated in Figure 4, a characteristic fourfold peak with an intensity ratio of 1:2:2:1 was observed, indicative of $\bullet\text{OH}$ production in both the EC-PMS-BDD and EC-PMS-DSA processes. However, the signal attributed to DMPO- $\text{SO}_4^{\bullet-}$ during the EC-PMS-DSA process was relatively weak, likely due to the rapid conversion of $\text{SO}_4^{\bullet-}$ to $\bullet\text{OH}$ through nucleophilic substitution [58].

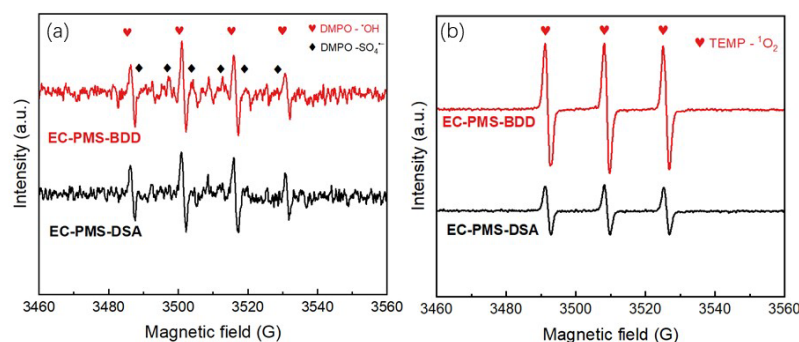


Figure 4. EPR spectrum of (a) DMPO- $\bullet\text{OH}$ and DMPO- $\text{SO}_4^{\bullet-}$ and (b) TEMP- $^1\text{O}_2$ obtained from both the EC-PMS-BDD and EC-PMS-DSA processes. Reaction conditions: $[\text{MNZ}] = 80 \mu\text{mol}\cdot\text{L}^{-1}$, $[\text{Na}_2\text{SO}_4] = 20 \text{mmol}\cdot\text{L}^{-1}$, $\text{pH}_0 = 6$, $I = 33.3 \text{mA}\cdot\text{cm}^{-2}$, and $[\text{PMS}] = 1 \text{mmol}\cdot\text{L}^{-1}$.

Additionally, a typical three-line spectrum with equal intensities was obtained, suggesting the formation of $^1\text{O}_2$ during the EC process. Moreover, the EC-PMS-BDD system exhibited a stronger signal of TEMP- $^1\text{O}_2$ compared to the EC-PMS-DSA system, indicating a higher concentration of $^1\text{O}_2$ in the EC-PMS-BDD system. This difference in $^1\text{O}_2$ concentration could be considered a contributing factor to the higher degradation efficiency observed in the EC-PMS-BDD system.

3.4.2. Quenching Experiments

To dig deeper into the involvement of different active radicals, radical scavengers were used to elucidate the degradation mechanism. Typically, ethanol was utilized to scavenge

both $\bullet\text{OH}$ and $\text{SO}_4^{\bullet-}$, whereas tert-butyl alcohol (TBA) was specifically employed as a scavenger of $\bullet\text{OH}$ [57]. Furthermore, ferrous formamidinate (FFA) serves as an indicator of $^1\text{O}_2$ and $\bullet\text{OH}$, with quenching rate constants of $1.2 \times 10^8 \text{ M}^{-1}\text{S}^{-1}$ and $1.5 \times 10^{10} \text{ M}^{-1}\text{S}^{-1}$, respectively [59,60]. Additionally, L-histidine functions as a scavenger of $^1\text{O}_2$ [61]. Quenching experiments were conducted using ethanol, TBA, FFA, and L-histidine to discern the dominant reactive oxygen species driving MNZ degradation in both the EC-PMS-BDD and EC-PMS-DSA processes (Figure S4a,b).

As depicted in Figure 5a, MNZ was completely removed within 45 min without scavengers during the PMS activation by electricity. However, the removal efficiency of MNZ decreased with the addition of TBA ($500 \text{ mmol}\cdot\text{L}^{-1}$), ethanol ($500 \text{ mmol}\cdot\text{L}^{-1}$), and FFA ($2 \text{ mmol}\cdot\text{L}^{-1}$), reaching 80.6%, 82.4%, and 82.3%, respectively. These findings suggest that while $\bullet\text{OH}$ and $\text{SO}_4^{\bullet-}$ are involved in the degradation process, they may not be the predominant reactive oxygen species. Moreover, ethanol (17.6%) exhibited a weaker inhibitory effect compared to TBA (19.4%), possibly due to TBA's greater likelihood of adsorption onto the surface of the BDD anode [54]. Notably, the addition of L-histidine ($20 \text{ mmol}\cdot\text{L}^{-1}$) quenched MNZ removal, reducing the removal efficiency to 60.3%, and the rate constant also decreased from 0.111 to 0.020 min^{-1} (Figure S4c), indicating that $^1\text{O}_2$ may indeed be the dominant reactive radical in the EC-PMS-BDD system.

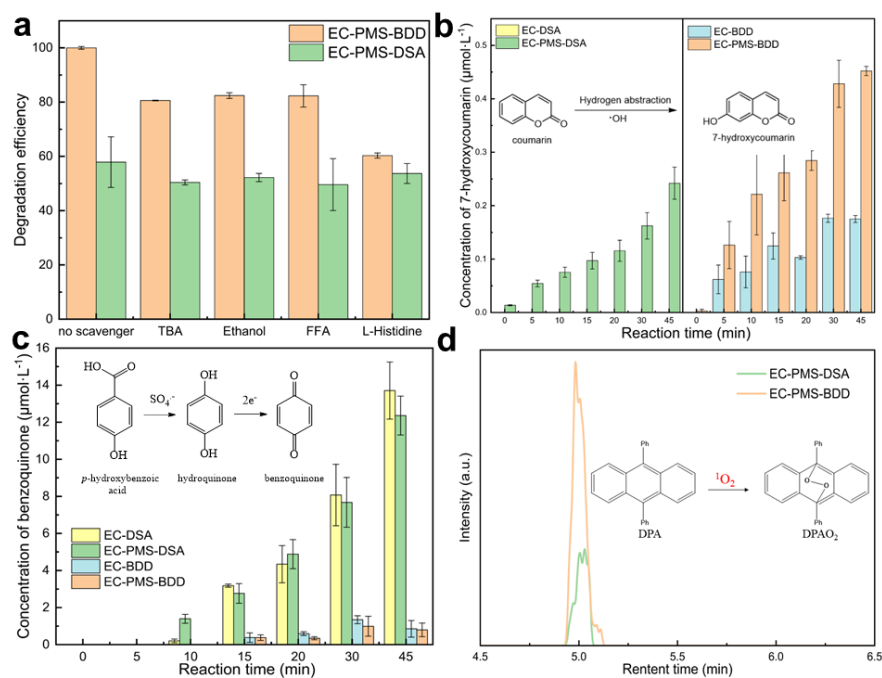


Figure 5. (a) Comparison of effects on degradation efficiency between EC-PMS-BDD and EC-PMS-DSA system by the addition of TBA, ethanol, FFA, and L-Histidine; The probe experiments of (b) $\bullet\text{OH}$ (c) $\text{SO}_4^{\bullet-}$ and (d) $^1\text{O}_2$. Reaction conditions: $[\text{MNZ}] = 80 \text{ }\mu\text{mol}\cdot\text{L}^{-1}$, $[\text{Na}_2\text{SO}_4] = 20 \text{ mmol}\cdot\text{L}^{-1}$, $\text{pH}_0 = 6$, $I = 33.3 \text{ mA}/\text{cm}^2$, and $[\text{PMS}] = 1 \text{ mmol}\cdot\text{L}^{-1}$.

During the EC-PME-DSA process, the addition of FFA resulted in a decrease in MNZ removal efficiency from 57.9% to 49.6% (Figure 5a). Considering that FFA is also an indicator of $^1\text{O}_2$, these results underscore the non-negligible contribution of $^1\text{O}_2$ to MNZ degradation alongside electrolysis.

3.4.3. Chemical Probe Experiments

Chemical probe methods were employed to detect the presence of $\bullet\text{OH}$, $\text{SO}_4^{\bullet-}$, and $^1\text{O}_2$ in the systems. As illustrated in Figure 5b, evidence of $\bullet\text{OH}$ formation was observed using coumarin as the probe in both systems. The yields of $\bullet\text{OH}$ were quantified based on the concentration of 7-hydroxycoumarin (7-HC), a highly fluorescent compound detectable

by an HPLC fluorescence detector [62,63]. Thus, it was inferred that the concentration of $\bullet\text{OH}$ equated to the concentration of 7-HC. Within 45 min, the yields of $\bullet\text{OH}$ were $0.5 \mu\text{mol}\cdot\text{L}^{-1}$ in the EC-PMS-BDD process, while they were $0.2 \mu\text{mol}\cdot\text{L}^{-1}$ in the EC-PMS-DSA process. This suggests that the electrochemical process with BDD as the anode exhibited a relatively higher yield of $\bullet\text{OH}$ compared to the DSA anode. This disparity could be attributed to the high electrochemical activity of the BDD anode, enabling the production of $\bullet\text{OH}$ through water dissociation [64].

Moreover, the concentration of $\bullet\text{OH}$ in both the EC-PMS-BDD and EC-PMS-DSA systems surpassed that in the EC-BDD and EC-DSA systems, respectively, indicating that PMS activation significantly contributed to $\bullet\text{OH}$ production in PMS-based processes [46]. Notably, $\bullet\text{OH}$ was not detected in the EC-DSA process, potentially due to the minuscule production of $\bullet\text{OH}$, rendering it insufficient to react with coumarin.

Furthermore, the presence of $\text{SO}_4^{\bullet-}$ in the electrochemical systems was determined using *p*-hydroxybenzoic acid (*p*-HBA) as a chemical probe, which reacts with $\text{SO}_4^{\bullet-}$ to produce benzoquinone (BQ), which is a more stable byproduct converted from hydroquinone. As illustrated in Figure 5c, within a 45 min reaction time, the concentration of $\text{SO}_4^{\bullet-}$ in the EC-PMS-DSA process ($12.4 \mu\text{mol}\cdot\text{L}^{-1}$) exceeded that in the EC-PMS-BDD process ($0.8 \mu\text{mol}\cdot\text{L}^{-1}$). This trend was consistent with the observations in the EC-DSA and EC-BDD systems, suggesting a propensity for greater production or accumulation of $\text{SO}_4^{\bullet-}$ when DSA was utilized as the anode.

Ding et al. [65] proposed that PMS likely binds to the surface of the BDD anode, followed by its electrochemical activation to generate $\bullet\text{OH}$ and $\text{SO}_4^{\bullet-}$. The presence of sulfate ions as the electrolyte might induce competition for adsorption sites on the BDD surface between persulfate and sulfate ions, thereby inhibiting the conversion of persulfate to $\text{SO}_4^{\bullet-}$. This mechanism could explain the lower concentration of $\text{SO}_4^{\bullet-}$ observed when BDD was employed as the anode.

In addition, the yields of $\text{SO}_4^{\bullet-}$ in the EC-PMS-DSA ($12.4 \mu\text{mol}\cdot\text{L}^{-1}$) and EC-DSA ($13.7 \mu\text{mol}\cdot\text{L}^{-1}$) systems within 45 min clearly indicate that the presence of PMS inhibited the production of $\text{SO}_4^{\bullet-}$. This inhibition could be attributed to the reaction between PMS and $\text{SO}_4^{\bullet-}$ (Equation (12)), resulting in the formation of $\text{SO}_5^{\bullet-}$ and consequently leading to a slight decrease in $\text{SO}_4^{\bullet-}$ concentration [46,66].

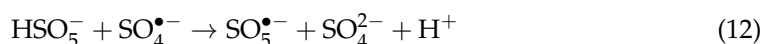


Figure 5d portrays the formation of DPAO_2 in the EC-PMS-DSA and EC-PMS-BDD systems as observed in the results of chemical probe experiments targeting $^1\text{O}_2$. In this experiment, 9,10-diphenyl anthracene (DPA) served as the $^1\text{O}_2$ quencher to detect the presence of $^1\text{O}_2$ [67]. As depicted in Figure 5d, a significantly higher peak intensity was discerned in the EC-PMS-BDD system, a trend consistent with the findings of the EPR test (Figure 4b).

These observations suggest that $^1\text{O}_2$ is indeed a significant radical, and the disparity in the quantity of $^1\text{O}_2$ between these two systems likely accounts for the divergent degradation efficiencies of MNZ.

3.5. Effects of Different Water Matrices

Anions (e.g., Cl^- , H_2PO_4^- , HCO_3^- , etc.) are commonly present in natural water matrices and can exert influence on the degradation of various contaminants. Therefore, it is crucial to investigate the effects of different concentrations of these anions on the removal of MNZ using the EC-PMS-BDD system.

3.5.1. Effect of Cl^- Addition

The effect of Cl^- on MNZ degradation was investigated, as shown in Figure 6a. The removal efficiency increased from 86.6% in the absence of Cl^- to 99.1%, 98.7%, and 96.7% with concentrations of 1, 5, and 10 $\text{mmol}\cdot\text{L}^{-1}$, respectively, at 30 min. This enhancement can be elucidated using two mechanisms.

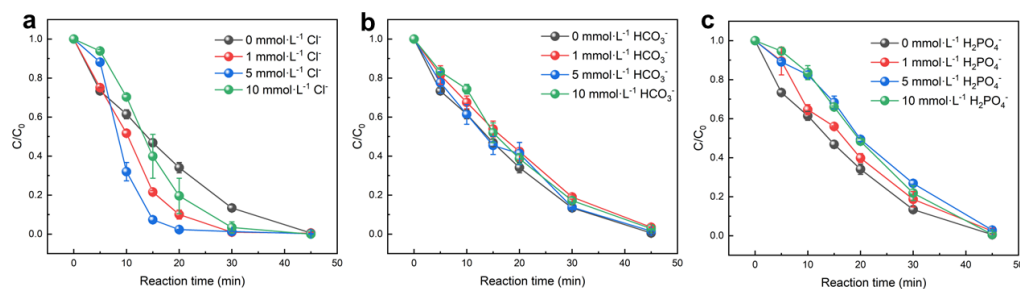


Figure 6. Effects of anions: (a) Cl^- , (b) HCO_3^- , and (c) H_2PO_4^- . Reaction conditions: $[\text{MNZ}] = 80 \mu\text{mol}\cdot\text{L}^{-1}$, $[\text{Na}_2\text{SO}_4] = 20 \text{mmol}\cdot\text{L}^{-1}$, initial pH = 6, $I = 33.3 \text{mA}\cdot\text{cm}^{-2}$, and $[\text{PMS}] = 1 \text{mmol}\cdot\text{L}^{-1}$.

Firstly, Cl^- ions could undergo oxidation to produce Cl_2 , which in turn reacts with water to generate free chlorine species such as hypochlorous acid (HOCl) and hypochlorite ions (ClO^-), as described by the following reactions (Equations (13) and (14)). These species are known to accelerate the degradation of MNZ [13,68,69].

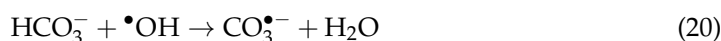
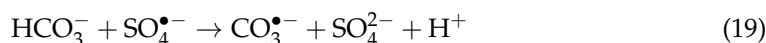


Secondly, Cl^- can also participate in the degradation process by reacting with $\bullet\text{OH}$ and $\text{SO}_4^{\bullet-}$ to produce Cl^\bullet through the reactions outlined in Equations (15)–(17) [70]. Subsequently, Cl^\bullet can further react with Cl^- to form chlorine dioxide radical anions ($\text{Cl}_2^{\bullet-}$), as depicted in Equation (18) [71]. It has been demonstrated that both Cl^\bullet and $\text{Cl}_2^{\bullet-}$ species can enhance the degradation of organic pollutants [49].



3.5.2. Effect of HCO_3^- Addition

Different concentrations of HCO_3^- were introduced to examine their impact on MNZ removal, as illustrated in Figure 6b. The removal efficiency decreased from 86.6% in the absence of HCO_3^- to 81.0% with a concentration of $10 \text{mmol}\cdot\text{L}^{-1}$ at 30 min, indicating that the degradation of MNZ was hindered in the presence of HCO_3^- . This outcome can be attributed to the scavenging action of HCO_3^- on free radicals, resulting in the production of less reactive $\text{CO}_3^{\bullet-}$, as depicted in Equations (19) and (20) [49].



Furthermore, the marginal impact of increasing the HCO_3^- concentration to 5 or $10 \text{mmol}\cdot\text{L}^{-1}$ on MNZ decomposition could be attributed to the alteration of pH resulting from the excess HCO_3^- . This observation aligns with the findings regarding the effect of pH on MNZ removal. The addition of excess HCO_3^- elevated the solution pH, consequently facilitating the degradation of MNZ.

3.5.3. Effect of H_2PO_4^- Addition

Figure 6c illustrates the impact of H_2PO_4^- on the degradation of MNZ. The removal efficiency of MNZ decreased from 86.6% to 81.3%, 73.2%, and 78.2% as the concentration of

H_2PO_4^- increased from 0 to 1, 5, and 10 $\text{mmol}\cdot\text{L}^{-1}$, respectively, at 30 min. These findings suggest that H_2PO_4^- may not be conducive to the activation of PMS, which is in line with previous research investigating the use of phosphates to degrade sulfamethoxazole in an activated peroxymonosulfate system [72]. Moreover, it is likely that the energy barrier for PMS activation by H_2PO_4^- is prohibitively high, making it difficult to effectively activate PMS [72,73].

3.6. Analysis of MNZ Byproducts

3.6.1. Proposed Pathway of MNZ Degradation

To investigate deeper into the potential degradation pathways of MNZ within the EC-PMS-BDD system, a multifaceted approach was undertaken. UPLC-MS spectra of the intermediate products were generated based on the findings of UHPLC-QTOF-MS analysis. Furthermore, the highest occupied molecular orbital (HOMO) was utilized to depict electron density transitions within MNZ molecules (Figures S5–S8). Additionally, the Fukui index was employed to elucidate active sites on the molecules (Figure S5).

As depicted in Figure 7, three plausible removal pathways of MNZ were identified as follows: (I) The oxidation of the N-ethanol group into carboxyl led to the formation of P1, identified as (2-methyl-5-nitroimidazol-1-yl) acetic acid. Subsequently, the loss of the N-acetic acid group from P1 resulted in the generation of P2, identified as 2-methyl-5-nitro-1H-imidazole [74]. This observation aligns with the proposition that the high electron density located at the nitrogen atom of P1 renders it susceptible to attack by reactive radicals, as indicated by the HOMO of P1 (Figure S6). Additionally, P3 was obtained through the loss of the nitro group, followed by the opening of the imidazole moiety to yield P4. (II) Reactive radicals can attack MNZ to reduce the nitro group, resulting in the formation of P5 and P6. P7 is subsequently generated from P6 through an imidazole ring opening [75]. As depicted by the HOMO of P6 in Figure S7, the C-C double bond outside the imidazole ring is attacked due to its high electron density, resulting in the conversion of P6 into chain organic compounds. These intermediates have also been identified in previous studies [75]. (III) MNZ undergoes denitration and oxidation, leading to the formation of P8 via hydroxyl radical attack.

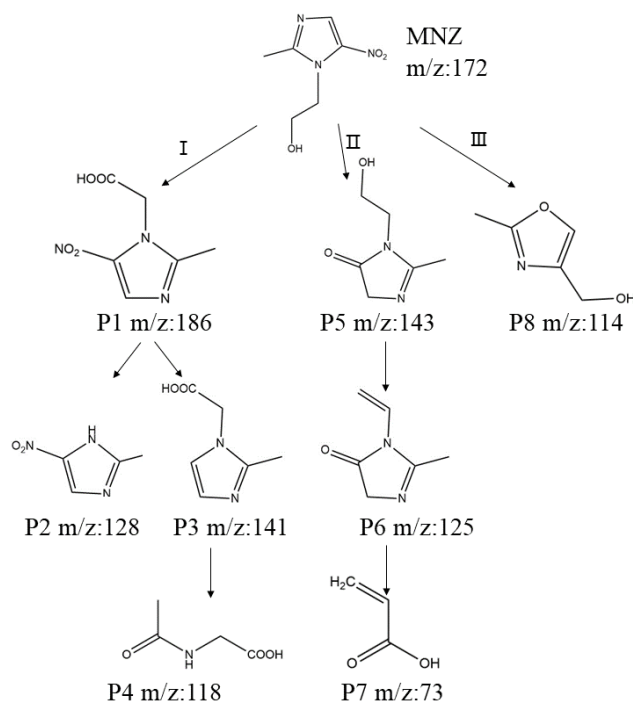


Figure 7. Proposed degradation pathway of MNZ in EC-PMS-BDD system.

3.6.2. Toxicity Evaluation

To assess the environmental implications of MNZ and its removal byproducts, various toxicity endpoints including acute toxicity, bioaccumulation factor, developmental toxicity, and mutagenicity were evaluated using the Toxicity Estimation Software Tool (T.E.S.T) v17.0.2.0 with quantitative structure–activity relationship (QSAR) models and hierarchical clustering forecasting methods.

As depicted in Figure 8a, the LD₅₀ values of P2, P3, P4, and P7 were determined to be 661.21 mg/kg, 681.63 mg/kg, 787.56 mg/kg, and 62.42 mg/kg, respectively. These values classify these byproducts as “toxic” since they are less than 1000 mg/kg.

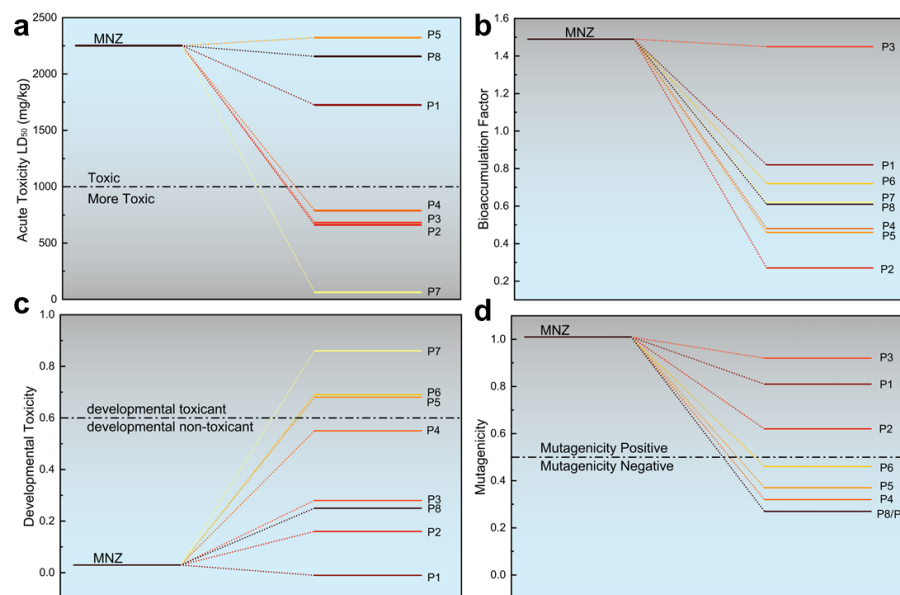


Figure 8. (a) Acute toxicity, (b) bioaccumulation factor, (c) developmental toxicity, and (d) mutagenicity of MNZ and byproducts in EC-PMS-BDD system. These values were calculated using the Toxicity Estimation Software Tool (T.E.S.T) using a quantitative structure–activity relationship prediction (QSAR) model.

Figure 8b illustrates that all the byproducts exhibited lower bioaccumulation factors compared to MNZ, suggesting a decrease in the bioaccumulation potential of the contaminant during degradation.

Regarding developmental toxicity, as shown in Figure 8c, MNZ is classified as a “developmental non-toxicant” with a developmental toxicity value of 0.03. However, most of the intermediates displayed an increasing trend in developmental toxicity, except for P1, which showed a value of -0.01 . Notably, the predictive results for P5, P6, and P7 with higher developmental toxicity values exceeding 0.6 indicate that these intermediates are considered “developmental toxicants.”

Furthermore, Figure 8d indicates that the mutagenicity value of MNZ was 1.01, which was higher than all the byproducts, suggesting a tendency for the mutagenicity of the pollutant to decline during the degradation process.

3.7. Removal Efficiency of Other Persistent Organic Pollutants

In order to demonstrate the superiority and universal applicability of the current water treatment approach, we also conducted degradation experiments against SMX, CBZ, and NB in addition to MNZ. This was to explore the applicability of the current method for the degradation of organic pollutants with either electron-donating groups or electron-withdrawing groups. As depicted in Figure 9, the organic pollutants SMX, CBZ, and NB were subjected to individual removal by the EC-PMS-BDD system, each starting with an initial concentration of $80 \mu\text{mol}\cdot\text{L}^{-1}$. The reaction rates of these target pollutants are

presented in Figure S9. Despite exhibiting similar reaction trends under the same system, the final degradation efficiencies varied. Specifically, the removal efficiency of CBZ reached 84.2% after 45 min, whereas that of SMX and NB was slightly lower at 69.1% and 71.4%, respectively. Although not as pronounced as the 99.5% removal achieved for MNZ, these results collectively demonstrate the effectiveness of the EC-PMS-BDD process in degrading various persistent organic pollutants.

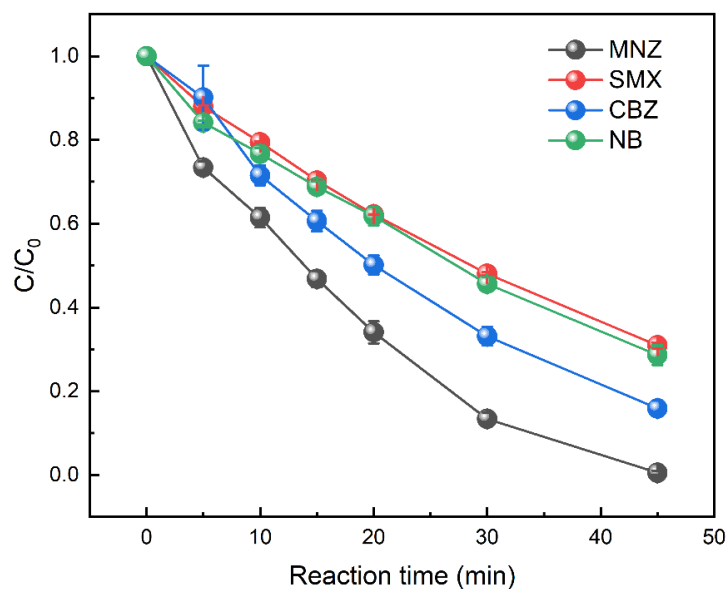


Figure 9. Removal of MNZ, SMX, CBZ, and NB by EC-PMS-BDD process. Reaction conditions: [Organic pollutants] = 80 $\mu\text{mol}\cdot\text{L}^{-1}$, $[\text{Na}_2\text{SO}_4]$ = 20 $\text{mmol}\cdot\text{L}^{-1}$, pH_0 = 6, [PMS] = 1 $\text{mmol}\cdot\text{L}^{-1}$, and I = 33.3 mA/cm^2 .

In the EC-PMS-BDD system, the electric energy per order (EE/O) serves as an effective parameter for estimating energy consumption. The calculation formula for EE/O is as follows:

$$\frac{\text{EE}}{\text{O}} = \frac{Pt \times 1000}{V \times 60 \times \lg\left(\frac{C_0}{C_t}\right)} \quad (21)$$

where P is the total current power (kW), t is the reaction time (min), V is the volume of the reaction system (L), C_0 is the initial concentration of MNZ, and C_t is the concentration of MNZ at t min. Equation (21) can be further deduced as follows:

$$\frac{\text{EE}}{\text{O}} = \frac{Pt \times 1000}{V \times 60 \times \lg\left(\frac{C_0}{C_t}\right)} = \frac{1000 \times Pt}{60 \times 0.4343 \times Vkt} = \frac{38.38P}{VK_{\text{obs}}} \quad (22)$$

where k_{obs} is the first-order apparent rate constant (min^{-1}).

The EE/O of SMX, CBZ, NB, and MNZ are shown in Table 5.

Table 5. Electric energy per order (EE/O) of SMX, CBZ, NB, and MNZ.

Pollutant	Current Intensity (A)	Voltage (V)	Volume (L)	Kobs (min^{-1})	EE/O (kWh m^3)
SMX	0.3	11.6	0.16	0.026	32.3
CBZ	0.3	11.8	0.16	0.041	20.6
NB	0.3	11.5	0.16	0.027	30.5
MNZ	0.3	11.7	0.16	0.111	7.6

4. Discussion

This study systematically investigated the synergistic effects of peroxymonosulfate (PMS) and electrochemical oxidation systems utilizing BDD or DSA electrodes, revealing an accelerated removal efficiency of MNZ. The efficiency of MNZ removal was observed to increase with an increase in the PMS dosage ranging from 1 mmol·L⁻¹ and current density ranging from 33.3 A/cm² while remaining stable within a specific pH range of around 6. And utilizing the Box–Behnken Design model, the conditions leading to the highest MNZ removal efficiency were obtained and discussed. Quenching experiments and chemical probe analyses confirmed the significant contribution of •OH, SO₄^{•-}, and ¹O₂, as well as the electrolysis mechanism, to the degradation of MNZ. Furthermore, it was determined that the presence of HCO₃⁻ and H₂PO₄⁻ inhibited MNZ removal, except for Cl⁻. The intermediates determination and T.E.S.T analysis provided meaningful support in the identification of byproducts to reveal diverse degradation pathways of MNZ in the EC-PMS-BDD system, specifically examining the environmental implications of the degradation process. Overall, this work demonstrated that the EC-PMS-BDD system exhibited superior potential, compared to the EC-PMS-DSA system, in the electrochemical activation of PMS for contaminant degradation, which, hence, furnishes a conceptual framework and guidance for devising strategies aimed at the treatment of medical wastewater.

Supplementary Materials: The following supporting information can be downloaded at: <https://www.mdpi.com/article/10.3390/en17071750/s1>, Figure S1. The concentration of PMS in EC-PMS-BDD and EC-PMS-DSA system. Reaction conditions: [MNZ] = 80 μmol·L⁻¹, [Na₂SO₄] = 20 mmol·L⁻¹, pH₀ = 6, I = 33.3 mA/cm². Figure S2. Effect of (a) current density, (b) initial pH, (c) PMS dosage on MNZ removal in EC-PMS-BDD system; effect of (d) current density, (e) initial pH, (f) PMS dosage on MNZ removal in EC-PMS-DSA system. Reaction conditions: [MNZ] = 80 μmol·L⁻¹, [Na₂SO₄] = 20 mmol·L⁻¹, pH₀ = 6, [PMS] = 1 mmol·L⁻¹, I = 33.3 mA/cm². Figure S3. The pseudo-first-order kinetics model on MNZ degradation of (a) current density, (b) initial pH, (c) PMS dosage in EC-PMS-BDD process; the pseudo-first-order kinetics model on MNZ degradation of (d) current density, (e) initial pH, (f) PMS dosage in EC-PMS-DSA process. Reaction conditions: [MNZ] = 80 μmol·L⁻¹, [Na₂SO₄] = 20 mmol·L⁻¹, pH₀ = 6, [PMS] = 1 mmol·L⁻¹, I = 33.3 mA/cm². Figure S4. Effects of TBA, Ethanol, FFA and L-Histidine on MNZ removal efficiency in (a) EC-PMS-BDD process and (b) EC-PMS-DSA process; (c) Pseudo-first-order kinetic constant under different scavengers in EC-PMS-BDD and EC-PMS-DSA process. Figure S5. (a) Identification of MNZ (m/z +172) and its fragment ions, and (b) the Fukui index of MNZ. Figure S6. (a) Identification of fragment ions 186 ([M+H]⁺), 128 ([M+H]⁺), 141 ([M+H]⁺), 118 ([M+H]⁺); (b) the degradation routes in pathway I. Figure S7. (a) Identification of fragment ions 143 ([M+H]⁺), 125 ([M+H]⁺), 73 ([M+H]⁺); (b) the degradation routes in pathway II. Figure S8. (a) Identification of fragment ions 114 ([M+H]⁺); (b) the degradation routes in pathway III. Figure S9. Pseudo-first-order kinetic constant of SMX, CBZ, NB and MNZ degradation in EC-PMS-BDD process. Figure S10. Schematic diagram of electrochemical oxidation system. Table S1. Parameters of HPLC methods for analysis of different compounds. Table S2. Actual values corresponding to coded levels of RSM. Table S3. 4-factor Box-Behnken design of RSM and experimental response. Table S4. ANOVA analysis for MNZ removal efficiency.

Author Contributions: Conceptualization, I.Y.Z. and R.H.; Methodology, H.L., J.F., X.L., I.Y.Z. and R.H.; Validation, H.L., J.F. and J.W.; Formal analysis, H.L. and J.F.; Investigation, H.L.; Data curation, J.F.; Writing—original draft, H.L. and R.H.; Writing—review & editing, J.W., X.L., I.Y.Z. and R.H.; Project administration, R.H.; Funding acquisition, R.H. All authors have read and agreed to the published version of the manuscript.

Funding: The authors would like to acknowledge “From 0 to 1” innovation technology project of Sichuan University (No. 2023SCUH0084) and the Special Funds for Scientific and Technological Collaboration of SCU-Zigong (No. 2022CDZG-3). This work was also supported by State Key Laboratory of Physical Chemistry of Solid Surfaces (No. 202105) in Xiamen University and Key Laboratory of Spectrochemical Analysis & Instrumentation (Xiamen University), Ministry of Education-SCAI2006.

Data Availability Statement: The original contributions presented in the study are included in the article/Supplementary Material, further inquiries can be directed to the corresponding author/s.

Conflicts of Interest: The authors declare no conflict of interest.

Appendix A

The target contaminant metronidazole (MNZ), and other organic pollutants, i.e., carbamazepine (CBZ, $\geq 98\%$), sulfamethoxazole (SMX, $\geq 98\%$), and nitrobenzene (NB, 99%) were purchased from Adamas-beta[®], Hangzhou, China. Peroxymonosulfate (PMS, $\text{KHSO}_5 \cdot 0.5\text{KHSO}_4 \cdot 0.5\text{K}_2\text{SO}_4$), sodium chloride (NaCl, $\geq 99.0\%$), sodium dihydrogen phosphate (Na_2HPO_4 , $\geq 99.0\%$), sodium bicarbonate (NaHCO_3 , $\geq 99.0\%$), sodium sulfate (Na_2SO_4 , $\geq 99.0\%$), hydrochloric acid (HCl), 5,5-dimethyl-1-pyrrolidine-N-oxide (DMPO), 2,2,6,6-tetramethyl-4-piperidinyloxyl (TEMP), scavengers tertbutyl alcohol (TBA, $\geq 99.5\%$), furfuryl alcohol (FFA, $\geq 98\%$), and L-Histidine were also obtained from Adamas-beta[®] of China. Sodium hydroxide (NaOH), sulfuric acid (H_2SO_4), and ethanol were obtained from the Chengdu Kelong chemical reagent factory (Chengdu, China). 2,2-azino-bis(3-ethylbenzothiazoline)-6-sulfonic acid diammonium (ABTS, 99%) was purchased from Sigma-Aldrich, Shanghai, China. All the reagents were of analytical grade and used without further purification. All solutions were prepared using ultrapure water.

Appendix B

Metronidazole (MNZ), sulfamethoxazole (SMX), carbamazepine (CBZ), nitrobenzene (NB), benzoic acid (BA), p-hydroxybenzoic acid (p-HBA), and p-benzoquinone (p-BQ) were measured using high-performance liquid chromatography (HPLC, 1260 Infinity, Agilent, Santa Clara, USA) equipped with the ultraviolet detector and the fluorescence detector. Other parameters are listed in Table S1.

References

1. Neghi, N.; Kumar, M.; Burkhalov, D. Synthesis and application of stable, reusable TiO_2 polymeric composites for photocatalytic removal of metronidazole: Removal kinetics and density functional analysis. *Chem. Eng. J.* **2019**, *359*, 963–975. [[CrossRef](#)]
2. Damodhar, U.; Reddy, M.V. Impact of pharmaceutical industry treated effluents on the water quality of river Uppanar, South east coast of India: A case study. *Appl. Water Sci.* **2013**, *3*, 501–514. [[CrossRef](#)]
3. Kummerer, K. Resistance in the environment. *J. Antimicrob. Chemother.* **2004**, *54*, 311–320. [[CrossRef](#)] [[PubMed](#)]
4. Moteshaker, P.; Rokni, S.; Farnoodian, N.; Mohassel Akhlaghi, N.; Saadi, S.; Ahmadidoust, G.; Yousefi, A. Application of response surface methodology for optimization of electrochemical process in metronidazole (MNZ) removal from aqueous solutions using stainless steel 316 (SS316) and lead (Pb) anodes. *Int. J. Chem. React. Eng.* **2020**, *18*, 20200055. [[CrossRef](#)]
5. Pan, Y.; Li, X.; Fu, K.; Deng, H.; Shi, J. Degradation of metronidazole by UV/chlorine treatment: Efficiency, mechanism, pathways and DBPs formation. *Chemosphere* **2019**, *224*, 228–236. [[CrossRef](#)] [[PubMed](#)]
6. Ding, C.; Fu, K.; Pan, Y.; Liu, J.; Deng, H.; Shi, J. Comparison of Ag and AgI-Modified ZnO as Heterogeneous Photocatalysts for Simulated Sunlight Driven Photodegradation of Metronidazole. *Catalysts* **2020**, *10*, 1097. [[CrossRef](#)]
7. Tian, W.; Gao, L.; Zhao, Y. Simultaneous determination of metronidazole, chloramphenicol and 10 sulfonamide residues in honey by LC-MS/MS. *Anal. Methods* **2013**, *5*, 1283–1288. [[CrossRef](#)]
8. Cai, H.; Ma, Z.; Zhao, T. Fabrication of magnetic CuFe_2O_4 @PBC composite and efficient removal of metronidazole by the photo-Fenton process in a wide pH range. *J. Environ. Manag.* **2021**, *300*, 113677. [[CrossRef](#)] [[PubMed](#)]
9. Cai, H.; Zhang, D.; Ma, X.; Ma, Z. A novel ZnO/biochar composite catalysts for visible light degradation of metronidazole. *Sep. Purif. Technol.* **2022**, *288*, 120633. [[CrossRef](#)]
10. Shah, A.; Shah, M. Characterisation and bioremediation of wastewater: A review exploring bioremediation as a sustainable technique for pharmaceutical wastewater. *Groundw. Sustain. Dev.* **2020**, *11*, 100383. [[CrossRef](#)]
11. Kitsiou, V.; Filippidis, N.; Mantzavinos, D.; Poullos, I. Heterogeneous and homogeneous photocatalytic degradation of the insecticide imidacloprid in aqueous solutions. *Appl. Catal. B Environ.* **2008**, *86*, 27–35. [[CrossRef](#)]
12. Hilla, S.; Kaçar, K.Y.; Linden, K.G. Degradation of the pharmaceutical metronidazole via UV, Fenton and photo-Fenton processes. *Chemosphere* **2006**, *63*, 269–276.
13. Cai, J.; Zhou, M.; Du, X.; Xu, X. Enhanced mechanism of 2,4-dichlorophenoxyacetic acid degradation by electrochemical activation of persulfate on Blue- TiO_2 nanotubes anode. *Sep. Purif. Technol.* **2021**, *254*, 117560. [[CrossRef](#)]
14. Deng, Y.; Zhao, R. Advanced Oxidation Processes (AOPs) in Wastewater Treatment. *Curr. Pollut. Rep.* **2015**, *1*, 167–176. [[CrossRef](#)]
15. Babu, D.S.; Srivastava, V.; Nidheesh, P.V.; Kumar, M. Detoxification of water and wastewater by advanced oxidation processes. *Sci. Total Environ.* **2019**, *696*, 133961. [[CrossRef](#)]
16. Jing, Q.; Yuzhu, X. Electrochemical oxidation technology: A review of its application in high-efficiency treatment of wastewater containing persistent organic pollutants. *J. Water Process Eng.* **2021**, *44*, 102308.

17. Radjenovic, J.; Sedlak, D.L. Challenges and Opportunities for Electrochemical Processes as Next-Generation Technologies for the Treatment of Contaminated Water. *Environ. Sci. Technol.* **2015**, *49*, 11292–11302. [[CrossRef](#)] [[PubMed](#)]
18. Mandal, P.; Yadav, M.; Gupta, A.K.; Dubey, B.K. Chlorine mediated indirect electro-oxidation of ammonia using non-active PbO₂ anode: Influencing parameters and mechanism identification. *Sep. Purif. Technol.* **2020**, *247*, 116910. [[CrossRef](#)]
19. Wang, J.; Yao, J.; Wang, L.; Xue, Q.; Hu, Z.; Pan, B. Multivariate optimization of the pulse electrochemical oxidation for treating recalcitrant dye wastewater. *Sep. Purif. Technol.* **2020**, *230*, 115851. [[CrossRef](#)]
20. Anglada, A.; Urriaga, A.; Ortiz, I. Contributions of electrochemical oxidation to waste-water treatment: Fundamentals and review of applications. *J. Chem. Technol. Biotechnol.* **2009**, *84*, 1747–1755. [[CrossRef](#)]
21. Fernandes, A.; Makoś, P.; Boczkaj, G. Treatment of bitumen post oxidative effluents by sulfate radicals based advanced oxidation processes (S-AOPs) under alkaline pH conditions. *J. Clean. Prod.* **2018**, *195*, 374–384. [[CrossRef](#)]
22. Boczkaj, G.; Fernandes, A. Wastewater treatment by means of advanced oxidation processes at basic pH conditions: A review. *Chem. Eng. J.* **2017**, *320*, 608–633. [[CrossRef](#)]
23. Rastogi, A.; Al-Abed, S.R.; Dionysiou, D.D. Sulfate radical-based ferrous–peroxymonosulfate oxidative system for PCBs degradation in aqueous and sediment systems. *Appl. Catal. B Environ.* **2008**, *85*, 171–179. [[CrossRef](#)]
24. Jie, Y.; Yan, Z.; Zekun, D. Enhanced degradation of contaminants of emerging concern by electrochemically activated peroxy-monosulfate: Performance, mechanism, and influencing factors. *Chem. Eng. J.* **2021**, *415*, 128938.
25. Li, X.Y.; Tang, S.; Yuan, D.; Tang, J.; Zhang, C.; Li, N.; Rao, Y. Improved degradation of anthraquinone dye by electrochemical activation of PDS. *Ecotoxicol. Environ. Saf.* **2019**, *177*, 77–85. [[CrossRef](#)] [[PubMed](#)]
26. Yang, S.; Wang, P.; Yang, X.; Shan, L.; Zhang, W.; Shao, X.; Niu, R. Degradation efficiencies of azo dye Acid Orange 7 by the interaction of heat, UV and anions with common oxidants: Persulfate, peroxy-monosulfate and hydrogen peroxide. *J. Hazard. Mater.* **2010**, *179*, 552–558. [[CrossRef](#)] [[PubMed](#)]
27. Hazime, R.; Nguyen, Q.H.; Ferronato, C.; Salvador, A.; Jaber, F.; Chovelon, J. Comparative study of imazalil degradation in three systems: UV/TiO₂, UV/K₂S₂O₈ and UV/TiO₂/K₂S₂O₈. *Appl. Catal. B Environ.* **2014**, *144*, 286–291. [[CrossRef](#)]
28. Ao, X.; Liu, W.; Sun, W.; Cai, M.; Ye, Z.; Yang, C.; Lu, Z.; Li, C. Medium pressure UV-activated peroxy-monosulfate for ciprofloxacin degradation: Kinetics, mechanism, and genotoxicity. *Chem. Eng. J.* **2018**, *345*, 87–97. [[CrossRef](#)]
29. Yang, Q.; Ma, Y.; Chen, F.; Yao, F.; Sun, J.; Wang, S.; Yi, K.; Hou, L.; Li, X.; Wang, D. Recent advances in photo-activated sulfate radical-advanced oxidation process (SR-AOP) for refractory organic pollutants removal in water. *Chem. Eng. J.* **2019**, *378*, 122149. [[CrossRef](#)]
30. Lominchar, M.A.; Santos, A.; De Miguel, E.; Romero, A. Remediation of aged diesel contaminated soil by alkaline activated persulfate. *Sci. Total Environ.* **2018**, *622*, 41–48. [[CrossRef](#)]
31. Ding, Y.; Zhu, L.; Wang, N.; Tang, H. Sulfate radicals induced degradation of tetrabromobisphenol A with nanoscaled magnetic CuFe₂O₄ as a heterogeneous catalyst of peroxy-monosulfate. *Appl. Catal. B Environ.* **2013**, *129*, 153–162. [[CrossRef](#)]
32. Sun, Z.; Liu, X.; Dong, X.; Zhang, X.; Tan, Y.; Yuan, F.; Zheng, S.; Li, C. Synergistic activation of peroxy-monosulfate via in situ growth FeCO₂O₄ nanoparticles on natural rectorite: Role of transition metal ions and hydroxyl groups. *Chemosphere* **2021**, *263*, 127965. [[CrossRef](#)] [[PubMed](#)]
33. Wang, J.B.H.; Yang, M.; Liu, R.; Hu, C.; Liu, H.; Qu, J. Anaerobically-digested sludge disintegration by transition metal ions-activated peroxy-monosulfate (PMS): Comparison between Co²⁺, Cu²⁺, Fe²⁺ and Mn²⁺. *Sci. Total Environ.* **2020**, *713*, 136530. [[CrossRef](#)]
34. Gujar, S.K.; Divyapriya, G.; Gogate, P.R.; Nidheesh, P.V. Environmental applications of ultrasound activated persulfate/peroxy-monosulfate oxidation process in combination with other activating agents. *Crit. Rev. Environ. Sci. Technol.* **2023**, *53*, 780–802. [[CrossRef](#)]
35. Xu, L.; Zhou, X.; Wang, G.; Zhou, L.; Sun, X. Catalytic degradation of acid red B in the system of ultrasound/peroxy-monosulfate/Fe₃O₄. *Sep. Purif. Technol.* **2021**, *276*, 119417. [[CrossRef](#)]
36. Jaesang, L.; Urs, V.G.; Jae-Hong, K. Persulfate-Based Advanced Oxidation: Critical Assessment of Opportunities and Roadblocks. *Environ. Sci. Technol.* **2020**, *54*, 3064–3081.
37. Waclawek, S.; Lutze, H.V.; Grübel, K.; Padil, V.V.; Černík, M.; Dionysiou, D.D. Chemistry of persulfates in water and wastewater treatment: A review. *Chem. Eng. J.* **2017**, *330*, 44–62. [[CrossRef](#)]
38. Ghanbari, F.; Moradi, M. Application of peroxy-monosulfate and its activation methods for degradation of environmental organic pollutants: Review. *Chem. Eng. J.* **2016**, *310*, 41–62. [[CrossRef](#)]
39. Song, H.; Yan, L.; Jiang, J.; Ma, J.; Zhang, Z.; Zhang, J.; Liu, P.; Yang, T. Electrochemical activation of persulfates at BDD anode: Radical or nonradical oxidation? *Water Res.* **2018**, *128*, 393–401. [[CrossRef](#)]
40. Nguyen Tien, H.; Bui, D.N.; Manh, T.D.; Tram, N.T.; Ngo, V.D.; Mwazighe, F.M.; Hoang, H.Y.; Le, V.T. Electrochemical degradation of indigo carmine, P-nitrosodimethylaniline and clothianidin on a fabricated Ti/SnO₂-Sb/Co-βPbO₂ electrode: Roles of radicals, water matrices effects and performance. *Chemosphere* **2022**, *313*, 137352. [[CrossRef](#)]
41. Li, X.; Fan, S.; Jin, C.; Gao, M.; Zhao, Y.; Guo, L.; Ji, J.; She, Z. Electrochemical degradation of tetracycline hydrochloride in sulfate solutions on boron-doped diamond electrode: The accumulation and transformation of persulfate. *Chemosphere* **2022**, *305*, 135448. [[CrossRef](#)] [[PubMed](#)]
42. Li, X.Y.; Cui, Y.H.; Feng, Y.J.; Xie, Z.M.; Gu, J.D. Reaction pathways and mechanisms of the electrochemical degradation of phenol on different electrodes. *Water Res.* **2005**, *39*, 1972–1981. [[CrossRef](#)] [[PubMed](#)]

43. Christos, C. Electrocatalysis in the electrochemical conversion/combustion of organic pollutants for waste water treatment. *Electrochim. Acta* **1994**, *39*, 1857–1862.
44. Feng, Y.J.; Li, X.Y. Electro-catalytic oxidation of phenol on several metal-oxide electrodes in aqueous solution. *Water Res.* **2003**, *37*, 2399–2407. [[CrossRef](#)] [[PubMed](#)]
45. Simond, O.; Comninellis, C. Anodic oxidation of organics on Ti/IrO₂ anodes using Nafion(R) as electrolyte. *Electrochim. Acta* **1997**, *42*, 2013–2018. [[CrossRef](#)]
46. Long, X.; Huang, R.; Li, Y.; Wang, J.; Zhang, M.; Zhang, I.Y. Understanding the electro-cocatalytic peroxymonosulfate-based systems with BDD versus DSA anodes: Radical versus nonradical dominated degradation mechanisms. *Sep. Purif. Technol.* **2023**, *309*, 123120. [[CrossRef](#)]
47. Ganiyu, S.O.; El-Din, M.G. Insight into in-situ radical and non-radical oxidative degradation of organic compounds in complex real matrix during electrooxidation with boron doped diamond electrode: A case study of oil sands process water treatment. *Appl. Catal. B Environ.* **2020**, *279*, 119366. [[CrossRef](#)]
48. Farhat, A.; Keller, J.; Tait, S.; Radjenovic, J. Removal of Persistent Organic Contaminants by Electrochemically Activated Sulfate. *Environ. Sci. Technol.* **2015**, *49*, 14326–14333. [[CrossRef](#)]
49. Liu, Z.; Ding, H.; Zhao, C.; Wang, T.; Wang, P.; Dionysiou, D.D. Electrochemical activation of peroxymonosulfate with ACF cathode: Kinetics, influencing factors, mechanism, and application potential. *Water Res.* **2019**, *159*, 111–121. [[CrossRef](#)]
50. McBeath, S.T.; Wilkinson, D.P.; Graham, N.J.D. Application of boron-doped diamond electrodes for the anodic oxidation of pesticide micropollutants in a water treatment process: A critical review. *Environ. Sci. Water Res. Technol.* **2019**, *5*, 2090–2107. [[CrossRef](#)]
51. Tian, C.; Dai, C.; Tian, X.; Nie, Y.; Yang, C.; Li, Y. Effects of Lewis acid-base site and oxygen vacancy in MgAl minerals on peroxymonosulfate activation towards sulfamethoxazole degradation via radical and non-radical mechanism. *Sep. Purif. Technol.* **2022**, *286*, 120437. [[CrossRef](#)]
52. Li, C.X.; Wang, Y.J.; Chen, C.B.; Fu, X.Z.; Cui, S.; Lu, J.Y.; Liu, H.Q.; Li, W.W. Interactions between chlorophenols and peroxymonosulfate: pH dependency and reaction pathways. *Sci. Total Environ.* **2019**, *664*, 133–139. [[CrossRef](#)] [[PubMed](#)]
53. Zhou, Y.; Jiang, J.; Gao, Y.; Ma, J.; Pang, S.Y.; Li, J.; Lu, X.T.; Yuan, L.P. Activation of Peroxymonosulfate by Benzoquinone: A Novel Nonradical Oxidation Process. *Environ. Sci. Technol.* **2015**, *49*, 12941–12950. [[CrossRef](#)] [[PubMed](#)]
54. Zhang, H.; Wang, X.; Zhao, X.; Dong, Y.; Wang, W.; Wang, L. Dolomite as a low-cost peroxymonosulfate activator for the efficient degradation of tetracycline: Performance, mechanism and toxicity evolution. *J. Water Process Eng.* **2022**, *49*, 103110. [[CrossRef](#)]
55. Chu, Z.; Chen, T.; Liu, H.; Chen, D.; Zou, X.; Wang, H.; Sun, F.; Zhai, P.; Xia, M.; Liu, M. Degradation of norfloxacin by calcite activating peroxymonosulfate: Performance and mechanism. *Chemosphere* **2021**, *282*, 131091. [[CrossRef](#)] [[PubMed](#)]
56. Miao, F.; Liu, Z.; Kang, X.; Cheng, C.; Mao, X.; Li, R.; Lin, H.; Zhang, H. Electro-enhanced heterogeneous activation of peroxymonosulfate via acceleration of Fe(III)/Fe(II) redox cycle on Fe-B catalyst. *Electrochim. Acta* **2021**, *377*, 138073. [[CrossRef](#)]
57. You, W.; Li, Y.; He, D.; Zeng, Y.; Zhu, J.; You, X.; Wang, K.; Zhou, G.; Peng, G. Activation of peroxymonosulfate by pyrophosphate for the degradation of AO₇ at neutral pH. *Environ. Sci. Pollut. Res. Int.* **2022**, *29*, 47549–47560. [[CrossRef](#)] [[PubMed](#)]
58. Chen, C.; Sun, H.Y.; Zhang, S.; Su, X. Structure-property relationship and mechanism of peroxymonosulfate activation by nitrogen-doped biochar for organic contaminant oxidation. *Appl. Surf. Sci.* **2023**, *609*, 15294. [[CrossRef](#)]
59. Ji, Y.; Lu, J.; Wang, L.; Jiang, M.; Yang, Y.; Yang, P.; Zhou, L.; Ferronato, C.; Chovelon, J. Non-activated peroxymonosulfate oxidation of sulfonamide antibiotics in water: Kinetics, mechanisms, and implications for water treatment. *Water Res.* **2018**, *147*, 82–90. [[CrossRef](#)]
60. Hayat, W.; Zhang, Y.; Huang, S.; Hussain, I.; Huang, R. Insight into the degradation of methomyl in water by peroxymonosulfate. *J. Environ. Chem. Eng.* **2021**, *9*, 105358. [[CrossRef](#)]
61. Huang, Y.; Sheng, B.; Wang, Z.; Liu, Q.; Yuan, R.; Xiao, D.; Liu, J. Deciphering the degradation/chlorination mechanisms of maleic acid in the Fe(II)/peroxymonosulfate process: An often overlooked effect of chloride. *Water Res.* **2018**, *145*, 453–463. [[CrossRef](#)] [[PubMed](#)]
62. Guo, L.; Jing, Y.; Chaplin, B.P. Development and Characterization of Ultrafiltration TiO₂ Magneli Phase Reactive Electrochemical Membranes. *Environ. Sci. Technol.* **2016**, *50*, 1428–1436. [[CrossRef](#)] [[PubMed](#)]
63. Guinea, E.; Arias, C.; Cabot, P.L.; Garrido, J.A.; Rodríguez, R.M.; Centellas, F.; Brillas, E. Mineralization of salicylic acid in acidic aqueous medium by electrochemical advanced oxidation processes using platinum and boron-doped diamond as anode and cathodically generated hydrogen peroxide. *Water Res.* **2008**, *42*, 499–511. [[CrossRef](#)] [[PubMed](#)]
64. Ganiyu, S.O.; Martinez-Huitle, C.A. Nature, Mechanisms and Reactivity of Electrogenerated Reactive Species at Thin-Film Boron-Doped Diamond (BDD) Electrodes During Electrochemical Wastewater Treatment. *Chemelectrochem* **2019**, *6*, 2379–2392. [[CrossRef](#)]
65. Ding, J.; Bu, L.; Zhao, Q.; Kabutey, F.T.; Wei, L.; Dionysiou, D.D. Electrochemical activation of persulfate on BDD and DSA anodes: Electrolyte influence, kinetics and mechanisms in the degradation of bisphenol A. *J. Hazard. Mater.* **2020**, *388*, 121789. [[CrossRef](#)] [[PubMed](#)]
66. Cheng, C.; Gao, S.; Zhu, J.; Wang, G.; Wang, L.; Xia, X. Enhanced performance of LaFeO₃ perovskite for peroxymonosulfate activation through strontium doping towards 2,4-D degradation. *Chem. Eng. J.* **2020**, *384*, 123377. [[CrossRef](#)]
67. Jayla, M.; Ju, Y.Y.; Jeanluc, A.A. Estimation of Singlet Oxygen Quantum Yield Using Novel Green-Absorbing Baird-type Aromatic Photosensitizers. *Photochem. Photobiol.* **2021**, *98*, 57–61.

68. Zhou, R.; Liu, F.; Xinyuan, D.; Zhang, C.; Yang, C.; Offiong, N.O.; Bi, Y.; Zeng, W.; Ren, H. Removal of metronidazole from wastewater by electrocoagulation with chloride ions electrolyte: The role of reactive chlorine species and process optimization. *Sep. Purif. Technol.* **2022**, *290*, 120799. [[CrossRef](#)]
69. Soufan, M.; Deborde, M.; Delmont, A.; Legube, B. Aqueous chlorination of carbamazepine: Kinetic study and transformation product identification. *Water Res.* **2013**, *47*, 5076–5087. [[CrossRef](#)]
70. Yu, X.Y.; Bao, Z.C.; Barker, J.R. Free Radical Reactions Involving Cl^\bullet , $\text{Cl}_2^{-\bullet}$, and $\text{SO}_4^{-\bullet}$ in the 248 nm Photolysis of Aqueous Solutions Containing $\text{S}_2\text{O}_8^{2-}$ and Cl^- . *J. Phys. Chem. A* **2003**, *108*, 295–308. [[CrossRef](#)]
71. Yu, X.Y.; Barker, J.R. Hydrogen Peroxide Photolysis in Acidic Aqueous Solutions Containing Chloride Ions. II. Quantum Yield of $\text{HO}^\bullet(\text{Aq})$ Radicals. *J. Phys. Chem. A* **2003**, *107*, 1313–1324. [[CrossRef](#)]
72. Wang, C.; Wang, Y.; Yu, Y.; Cui, X.; Yan, B.; Song, Y.; Li, N.; Chen, G.; Wang, S. Effect of phosphates on oxidative species generation and sulfamethoxazole degradation in a pig manure derived biochar activated peroxymonosulfate system. *Sep. Purif. Technol.* **2022**, *295*, 121255. [[CrossRef](#)]
73. Duan, P.; Liu, X.; Liu, B.; Akram, M.; Li, Y.; Pan, J.; Yue, Q.; Gao, B.; Xu, X. Effect of phosphate on peroxymonosulfate activation: Accelerating generation of sulfate radical and underlying mechanism. *Appl. Catal. B Environ.* **2021**, *298*, 120532. [[CrossRef](#)]
74. Li, C.; Zhu, X.J.; Shanshan, Y.; Tian, S.; Li, Y.; Bo, L.; Pan, Z.; Li, H. Novel strategy for the efficient degradation of organic contaminants using porous graphite electrodes: Synergistic mechanism of anodic and cathodic reactions. *Chem. Eng. J.* **2022**, *429*, 132340. [[CrossRef](#)]
75. Tran, M.L.; Fu, C.; Juang, R. Removal of metronidazole by TiO_2 and ZnO photocatalysis: A comprehensive comparison of process optimization and transformation products. *Environ. Sci. Pollut. Res. Int.* **2018**, *25*, 28285–28295. [[CrossRef](#)]

Disclaimer/Publisher's Note: The statements, opinions and data contained in all publications are solely those of the individual author(s) and contributor(s) and not of MDPI and/or the editor(s). MDPI and/or the editor(s) disclaim responsibility for any injury to people or property resulting from any ideas, methods, instructions or products referred to in the content.